



## OPEN

# High-Directivity Emissions with Flexible Beam Numbers and Beam Directions Using Gradient-Refractive-Index Fractal Metamaterial

He-Xiu Xu<sup>1,2</sup>, Guang-Ming Wang<sup>2</sup>, Zui Tao<sup>1</sup> & Tie Jun Cui<sup>1</sup><sup>1</sup>State Key Laboratory of Millimeter Waves, Department of Radio Engineering Southeast University, Nanjing 210096, China, <sup>2</sup>Missile institute, Air Force Engineering University, Xi'an 710051, China.

A three-dimensional (3D) highly-directive emission system is proposed to enable beam shaping and beam steering capabilities in wideband frequencies. It is composed of an omnidirectional source antenna and several 3D gradient-refractive-index (GRIN) lenses. To engineer a broadband impedance match, the design method for these 3D lenses is established under the scenario of free-space excitation by using a planar printed monopole. For realizations and demonstrations, a kind of GRIN metamaterial is proposed, which is constructed by non-uniform fractal geometries. Due to the non-resonant and deep-subwavelength features of the fractal elements, the resulting 3D GRIN metamaterial lenses have extra wide bandwidth (3 to 7.5 GHz), and are capable of manipulating electromagnetic wavefronts accurately, advancing the state of the art of available GRIN lenses. The proposal for the versatile highly-directive emissions has been confirmed by simulations and measurements, showing that not only the number of beams can be arbitrarily tailored but also the beam directions can be steerable. The proposal opens a new way to control broadband highly-directive emissions with pre-designed directions, promising great potentials in modern wireless communication systems.

Metamaterials, which contain a mass of artificial subwavelength unit cells, have sparked exponentially increased interest among scientists and engineers over the past decade due to the fantastic electromagnetic (EM) properties that are impossible to be achieved using natural materials. Since the initial motivation for scientific pursuit of negative refraction index in 2001<sup>1</sup>, physicists and engineers have pioneered new ways to guide and manipulate EM waves at will through appropriate choices and arrangements of meta-atoms (unit cells), giving rising to the directive<sup>2</sup> or enhanced<sup>3</sup> emissions, perfect imagings<sup>4-6</sup>, invisibility cloakings<sup>7-9</sup>, EM tunneling<sup>10</sup>, perfect absorbers<sup>11-14</sup>, and omnidirectional bending<sup>15</sup>, etc. In addition to the exhibited exciting phenomena in fundamental science, these conceptually new devices have broken the basic limitations for conventional devices, and thus provide an initial step towards unique functionalities. Nevertheless, the inherent drawbacks of large loss and limited bandwidth due to the resonant profiles of electric or magnetic inclusions as well as on occasion complicated fabrication process preclude applications of metamaterials in real world.

To our relief, gradient-refractive-index (GRIN) metamaterials<sup>16</sup> allow us to arbitrarily tailor the refractive index at the unit cell level in the frequencies well below resonances, and thus enable macroscopic EM responses with a set of new functionalities<sup>17,18</sup>. In the off-resonance region, the GRIN element exhibits required material properties in a wide band with negligible losses, advancing the state of the art of available metamaterials. Recent success in GRIN metamaterials has provided extreme controls over EM wavefronts across electrically thin layers, and thus facilitates an initial step towards Luneburg lenses, beam collimators, beam bendings, EM wave concentrators, illusion devices, microwave focusing, and highly-directive beam-scanning antennas<sup>19-37</sup>.

Despite these fruitful achievements, most previous reports were confined to the laboratory demonstration of the noted physics, for which the transverse-electric (TE) or transverse-magnetic (TM) polarized EM fields are examined extensively in a two-dimensional (2D) parallel-plate waveguide system<sup>19-33</sup>. Among them, the coaxial probe or point source was commonly employed as an ideal line source, which certainly conflicts with the free-space excitation in practice. Moreover, the homogenization of the GRIN materials can be further improved in terms of an effective medium. Most importantly, among the rarely reported three-dimensional (3D) lenses<sup>34-37</sup>,

## SUBJECT AREAS:

APPLIED PHYSICS

METAMATERIALS

ELECTRONIC DEVICES

ELECTRICAL AND ELECTRONIC  
ENGINEERING

Received

25 April 2014

Accepted

30 June 2014

Published

18 July 2014

Correspondence and requests for materials should be addressed to H.-X.X. (hxxuellen@gmail.com) or T.J.C. (tjcu@seu.edu.cn)

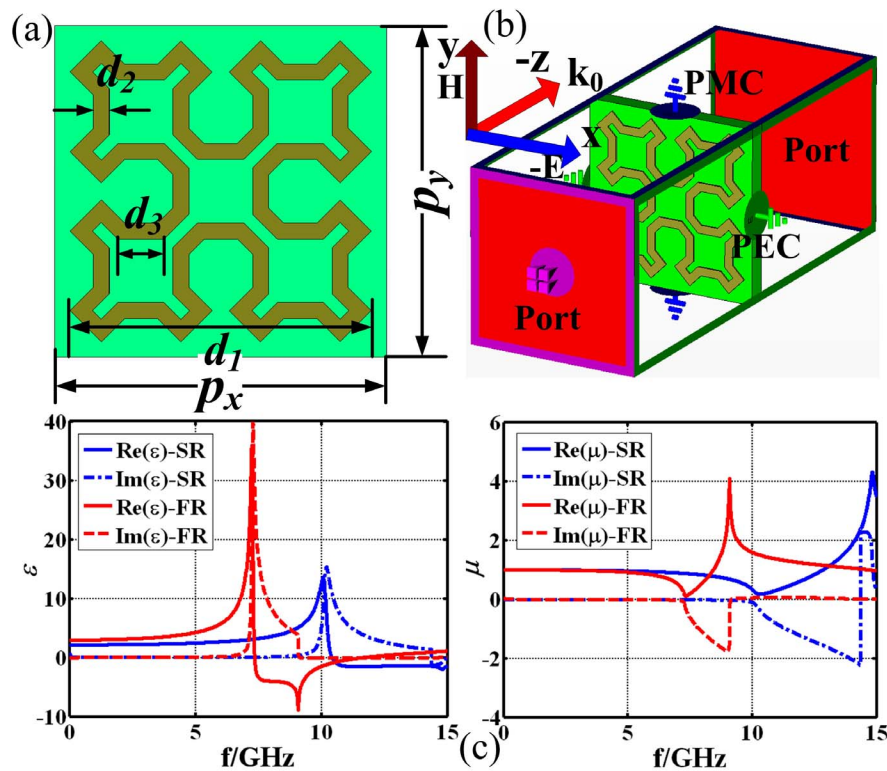


**Figure 1** | (a) Topology and (b) retrieved constitutive parameters of the proposed GRIN fractal element. The geometrical parameters of the Sierpinski fractal ring are given as  $d_1 = 7.56$  mm,  $d_2 = 0.4$  mm, and  $d_3 = 1.16$  mm when scale = 1.

the waveguide was exclusively adopted as the source and thus enabled only one desirable directive emission beam. This scheme to some extent deviates from the increasing demand on highly preferable directive emissions with flexible beam numbers and beam directions in a low-cost, low-weight and controllable manner. However, this 3D multi-beam highly-directive metamaterial lens antenna has not been reported yet so far.

In this article, the effective excitation and broadband impedance match of a 3D GRIN metamaterial lens were comprehensively explored under a wave launcher of an actual printed monopole. The lens was designed in free space instead of 2D mimicking in the parallel-plate waveguide where the electric or magnetic fields perpendicular to the 2D plane are constant. A kind of GRIN metamaterial element constructed based on closed Sierpinski fractal ring was proposed, studied, and then employed as a fundamental block to build the 3D collimating lens with satisfied index gradients. Due to the omnidirectional feature of the monopole, a multi-beam antenna system can be readily conceived by employing more lenses. The proposed scheme has been verified by a far-field measurement of four GRIN lenses embedded with a printed monopole. To the best of our knowledge, this is the first realization of a 3D antenna system with flexible beam numbers and beam directions for broadband highly-directive emissions of more than an octave.

## Results

**Characterization of GRIN fractal metamaterials.** The fractal scheme employed in this work is from the viewpoint of a much electrically smaller GRIN metamaterial element in virtue of the space-filling property, which is a new avenue advanced in material design<sup>5</sup>. Similar scheme has been employed to miniaturize the elements of composite right/left handed transmission line for a given resonant frequency<sup>38,39</sup>. The advantages of using rather a small element can be highlighted in twofold. First, the loading of one or two such elements may miniaturize considerably the planar circuits or antennas<sup>5</sup>,

which is an intriguing characteristic that meets the increasing demand on high integration of modern communication systems. Second, the volumetric structures made of these periodically arranged elements are more feasible to be described by the constitutive parameters under the framework of an effective medium<sup>40</sup> and the resulting collective EM response is less influenced by the parasitic diffraction effects, enabling the elements in metamaterials to be analogous to the atoms or molecules in natural materials. Therefore, a desirable EM functionality can be engineered accurately by tailoring the element structures, which would benefit considerably the design accuracy and success rate.

Fig. 1(a) shows the topology of the proposed GRIN metamaterial particle and its orientation with respect to the normally incident EM waves. The periodicity along  $x$ ,  $y$  and  $z$  axis is  $p_x$ ,  $p_y$ , and  $p_z$ , respectively. The GRIN element is made of a fractal ring (FR) etched on one side of the F4B board (leaving the other side unoccupied) with dielectric constant  $\epsilon_d = 2.65$ , thickness  $h = 0.3$  mm, and loss tangent  $\tan\sigma = 0.001$ . Due to the four-fold rotational symmetry of the FR in  $xoy$  plane, the GRIN element presents a planar isotropy and thus supports dual-polarization operation. In this particular design, the GRIN element is illuminated by a normally incident plane EM wave with polarization in the  $x$  direction, and the Sierpinski ring of the second-iteration order is utilized by taking a tradeoff between miniaturization and fabrications. Indeed, any zigzag fractal structure with strong space-filling property may benefit the compact design.

In the simulation setup shown in Fig. 1(b), the top-and-bottom boundaries of the GRIN element are assigned as perfectly magnetic conductors (PMC), whereas the left-and-right boundaries are set as perfectly electric conductors (PEC). The impinging electric field drives the line inductor in the  $x$  direction, and the gap capacitor (inter-ring coupling) formed between neighbouring FR structures as well as the capacitor formed between close neighbouring sections of the FR itself, facilitating an electric resonance modeled by a  $LC$  resonator which restores and discharges alternately. This can be



proved from Fig. S1 where the electric resonant frequency  $f_0 = 1/\sqrt{2\pi\sqrt{LC}}$  clearly shifts upwards as  $p_x$  and  $p_y$  increase simultaneously and appears to be saturated as  $p_x$  and  $p_y$  reach 9 mm. Although the decrease of  $p_x$  and  $p_y$  ensures increased gap capacitances, it either affords limited enhancement of capacitance or inherently brings about fabrication challenging and tolerances. Therefore, it is unadvisable to select this scheme to engineer a compact element.

Since the oscillating current forms and flows through the FR structure, the abnormal fractal zigzag boundary will succeed in extending the current path within a limited volume and thus efficiently lowers down the resonant frequency, enabling the element to be less than one-tenth of the working wavelength at  $f_0$ . To afford an efficient control over  $f_0$  in terms of variable inductors and capacitors in a simple manner, the Sierpinski ring is progressively scaled up and down by manipulating the scaling coefficient within a fixed lattice constant. In this regard, the effective parameters below  $f_0$  change accordingly and thus enable us to achieve a controllable arithmetical progression of refractive index.

To illustrate the effects of fractal perturbation, the reflection and transmission coefficients of the proposed GRIN fractal particle and its conventional counterpart using the square ring (SR)<sup>37</sup> are characterized by the commercial software CST Microwave Studio. For fair comparisons, both rings are with the same scaling coefficient 0.77 and both elements have the same lattice constant  $p_x \times p_y \times p_z = 6 \times 6 \times 6 \text{ mm}^3$ . These S-parameters (not shown for brevity of contents) are then utilized to retrieve the effective constitutive parameters using the standard retrieval procedure<sup>41</sup>, as shown in Fig. 1(c). As is observed in both cases, the permittivity curve undergoes an electric resonance around  $f_0$ , whereas the permeability curve suffers an anti-resonance. Moreover, an obvious frequency reduction of  $f_0$  near 2.9 GHz from 10.25 GHz to 7.34 GHz is inspected when the fractal geometry is introduced. Therefore, the GRIN fractal element obtains at least 28.3% size reduction for a given operation frequency. Moreover, the effective permittivity and permeability in both cases exhibit smooth slopes below  $f_0$  and the permittivity of the fractal element suffers a sharper and stronger resonance at  $f_0$ . As a consequence, the fractal element features larger index gradient with respect to its conventional counterpart.

**Broadband Highly-Directive Emission System.** Figs. 2(a)–(d) depict the topology and elaborated geometrical parameters of the proposed highly-directive emission system or in other words integrated lens antenna. As is shown, the antenna is composed of a broadband 3D GRIN collimating lens and an omnidirectional monopole to launch the lens. The distance from the monopole to the lens is  $D$ . Distinguished from the curved Fresnel lens which is often implemented by polystyrenes, the GRIN lens proposed here preserves flat surfaces and contains both core lens and coat lens (impedance matching layer)<sup>37</sup> to guarantee a wide operation band. Moreover, the GRIN lens is actualized by the proposed fractal metamaterials discussed previously, making current implementation distinguished from any earlier designs. Here, a planar microstrip trapezoid printed monopole deposited on a F4B substrate with  $\epsilon_d = 3.5$ ,  $h = 1.5 \text{ mm}$  and  $\tan\sigma = 0.001$  is explored as the source to achieve controllable uniform beams along several predicted directions with high integration, low weight, low cost, and broad band. To guarantee the bandwidth of the final antenna system, both the lens and monopole should operate in a wide band with fully overlapped frequencies. The wide bandwidth of the monopole is guaranteed by optimizing the geometrical parameters, whereas the design principle for a broadband lens is derived in the *Methods* section. Fig. 2(e) depicts the distributions of the theoretically calculated refractive index with discrete (solid line) and continuous (dashed line) profiles using the derived approach. As can be seen, the discrete index of the core lens varies gradually from 2.07 to 1.31, while that of the coat lens changes from 1.44 to 1.14. Notice that the discretized constitutive parameters have no penalty on lens function and performances<sup>21</sup> but enable the lens implementation more feasible and practical.

Although the inhomogeneous index gradient can be easily implemented by drilling isotropic holes in a dielectric slab<sup>36</sup>, the high fabrication cost, incompatibility with available printed circuit board (PCB) technology, and finite types of available aiguilles with discrete aperture dimensions limit the applications. Here, the proposed GRIN fractal particle is employed to realize the index gradient presented in Fig. 2(e) due to the unique EM response discussed in previous Section. Since the fractal element meets well the requirement for an effective medium and the material parameters exhibit a smooth dispersion in the off-resonant region, the undesirable distur-

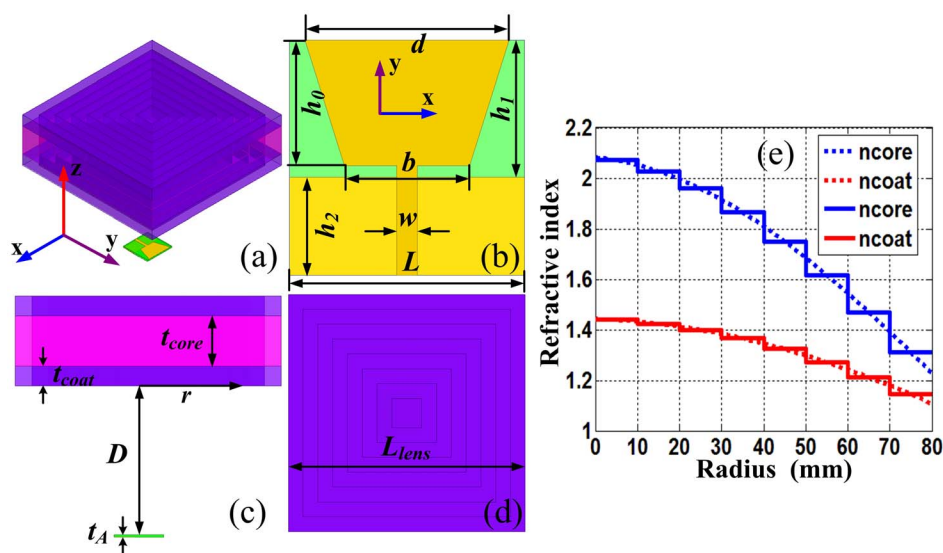


**Figure 2 | Topology and required index gradient of the broadband 3D GRIN lens antenna system.** (a) The perspective view of the system. (b) The illustration of monopole parameters. (c) The side view and (d) bottom view of the system. (e) The refractive index of the core and coat lens, in which  $t_{core} = 30 \text{ mm}$ ,  $t_{coat} = 12 \text{ mm}$ ,  $S = 90 \text{ mm}$ ,  $L_{lens} = 160 \text{ mm}$ ,  $t_A = 1.5 \text{ mm}$ ,  $L = 30 \text{ mm}$ ,  $w = 2.6 \text{ mm}$ ,  $h_0 = 16 \text{ mm}$ ,  $h_1 = 17.5 \text{ mm}$ ,  $h_2 = 12.5 \text{ mm}$ ,  $d = 26 \text{ mm}$ , and  $b = 16 \text{ mm}$ .

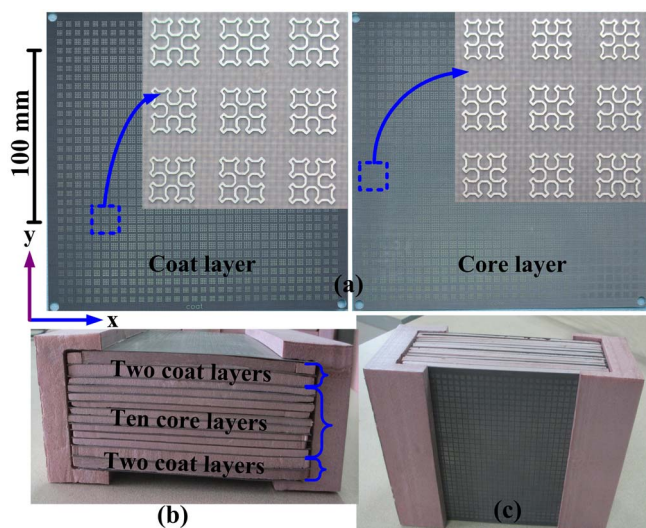


**Figure 3** | Photographs of the fabricated GRIN slab lens which occupies an area of  $170 \times 170 \times 54 \text{ mm}^3$ . (a) The coat layer and core layer. (b) The side view. (c) The perspective view.

tion of optical quality and significant impedance change between two adjacent layers suffered in traditional approach will be mitigated or completely eliminated. Moreover, the EM wave outgoing from the monopole illuminates the lens with normal incidence along  $z$  axis and polarization along  $y$  axis. This EM condition coincides well with that presented in Fig. 1(a), and thus will render the desirable electric response discussed previously, and in turn the efficient excitation of the resulting lens.

Here, several guidelines are highlighted for an easy design. First, the larger the lattice constant along the propagation is, the smaller index gradient and lower index values become. Second, the thicker the dielectric board is, the larger permittivity while smaller permeability are, leading to smaller index and deteriorative impedance matching. Finally, the larger  $\epsilon_d$  is, the larger  $n_r$  is. The unit cells of the core and coat lens are built on two kinds of F4B boards with  $(\epsilon_d, h, \tan\sigma) = (2.65, 0.5 \text{ mm}, 0.001)$  and  $(2.2, 0.5 \text{ mm}, 0.001)$ , corresponding to  $\lambda_0/12 \times \lambda_0/12 \times \lambda_0/20$  and  $\lambda_0/12 \times \lambda_0/12 \times \lambda_0/10$ , respectively. Here,  $\lambda_0$  is the working wavelength in free space at 5 GHz.

For design and characterization, the GRIN element, the lens, and the integrated antenna system are numerically evaluated in CST. The retrieved effective material parameters for the core and coat lens at 5.5 GHz are portrayed in Figs. S2 and S3, respectively. In both cases, the dimensions of FR sweep from scale = 0.4 to scale = 0.6 in steps of 0.001. Therein, we observe that the permittivity and refractive index vary continuously, while the permeability almost maintains at unity. Therefore, the dimensions of FR reduce gradually from the center to the edge of the lens. Moreover, the refractive index of the core lens increases progressively from 1.37 to 2.09 while that of the coat lens increases from 1.17 to 1.57. These index gradients completely fulfill the theoretical requirements for the lens. Most importantly, the imaginary parts of the permittivity, permeability and refractive index in both cases are negligible across the entire sweeping range, indicating a low loss.

Given the parametric sweeping results, the lens can be exactly constructed based on the geometrical mapping process using a root-finding algorithm. Fig. 3 depicts the photograph of the fabricated 3D GRIN lens which is composed of ten core layers sandwiched by two coat layers on each side. In the radial direction, each concentric region shown in Fig. 2(d) is realized by two GRIN elements with identical geometrical parameters. Hence a total of  $32 \times 32$  metallic patterns are positioned on either side of each F4B dielectric board. An additional 2.5-mm-thick foam plate with near-unity permeability and

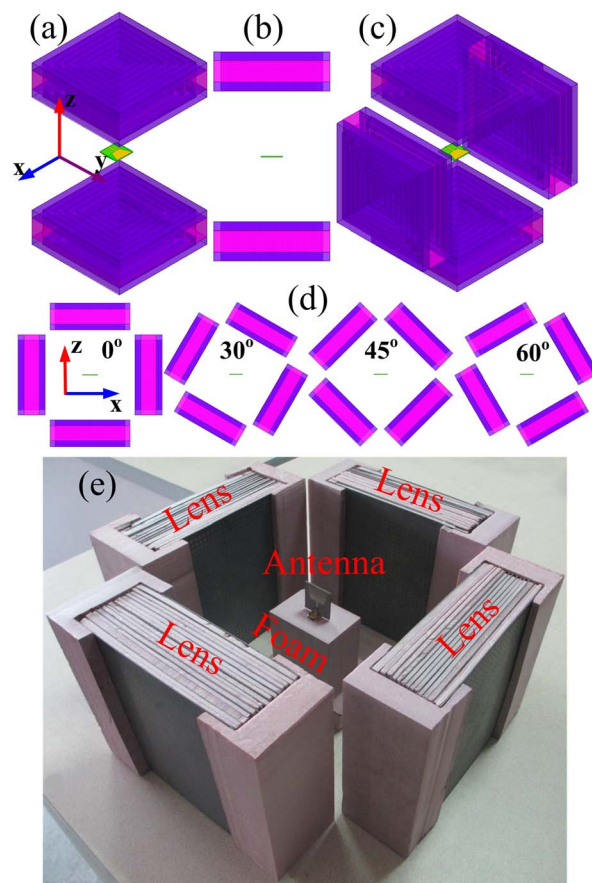


**Figure 4** | The scheme and prototype of the proposed multi-beam highly-directive emission systems. (a) The perspective view and (b) the side-view of a two-beam system. (c) The perspective view of a four-beam system. (d) The side-view of the four-beam systems, in which the four lenses are rotated by  $\theta = 0^\circ$ ,  $\theta = 30^\circ$ ,  $\theta = 45^\circ$ , and  $\theta = 60^\circ$ , respectively. (e) The prototype of the four-beam highly-directive emission system.

permittivity is placed between every two neighboring core layers to guarantee  $p_z = 3 \text{ mm}$ , whereas an additional 5.5-mm-thick foam plate is inserted between every two coat layers to guarantee  $p_z = 6 \text{ mm}$ . By tightly stacking these dielectric boards and foam plates alternatively and reinforcing them through adhesives, a 3D GRIN slab lens occupying an area of  $170 \times 170 \times 54 \text{ mm}^3$  is implemented. The lens is packaged in hand-made foam to provide supporting frame and can be made more compact when smaller index gradients or less concentric layers are used. However, this would either degrade the accuracy of lens implementation or deteriorate the lens performances.

The single-beam highly-directive emission system can be directly generalized to a multi-beam one. Fig. 4 illustrates the schematic of various multi-beam emission systems and the fabricated prototype of a four-beam lens antenna for demonstration. As can be seen, two or four GRIN lenses are arranged around the source monopole with identical  $D$ . The highly-directive emissions can be controlled in following four manners. First, the number of beams can be engineered arbitrarily by appropriately distributing more GRIN lenses. Second, the beam directions can be arbitrarily manipulated by tailoring the included angles between neighboring lenses. Third, the beams can be engineered rotated by placing the lenses on a mechanically rotated platform isochronous with a time sequence and fixing the feeding antenna. Finally, the beam can be tailored nonuniform by varying  $D$  and index gradient of the lenses. Here, the direction of beam is defined corresponding to the orientation angle  $\theta$  with respect to  $z$  axis.

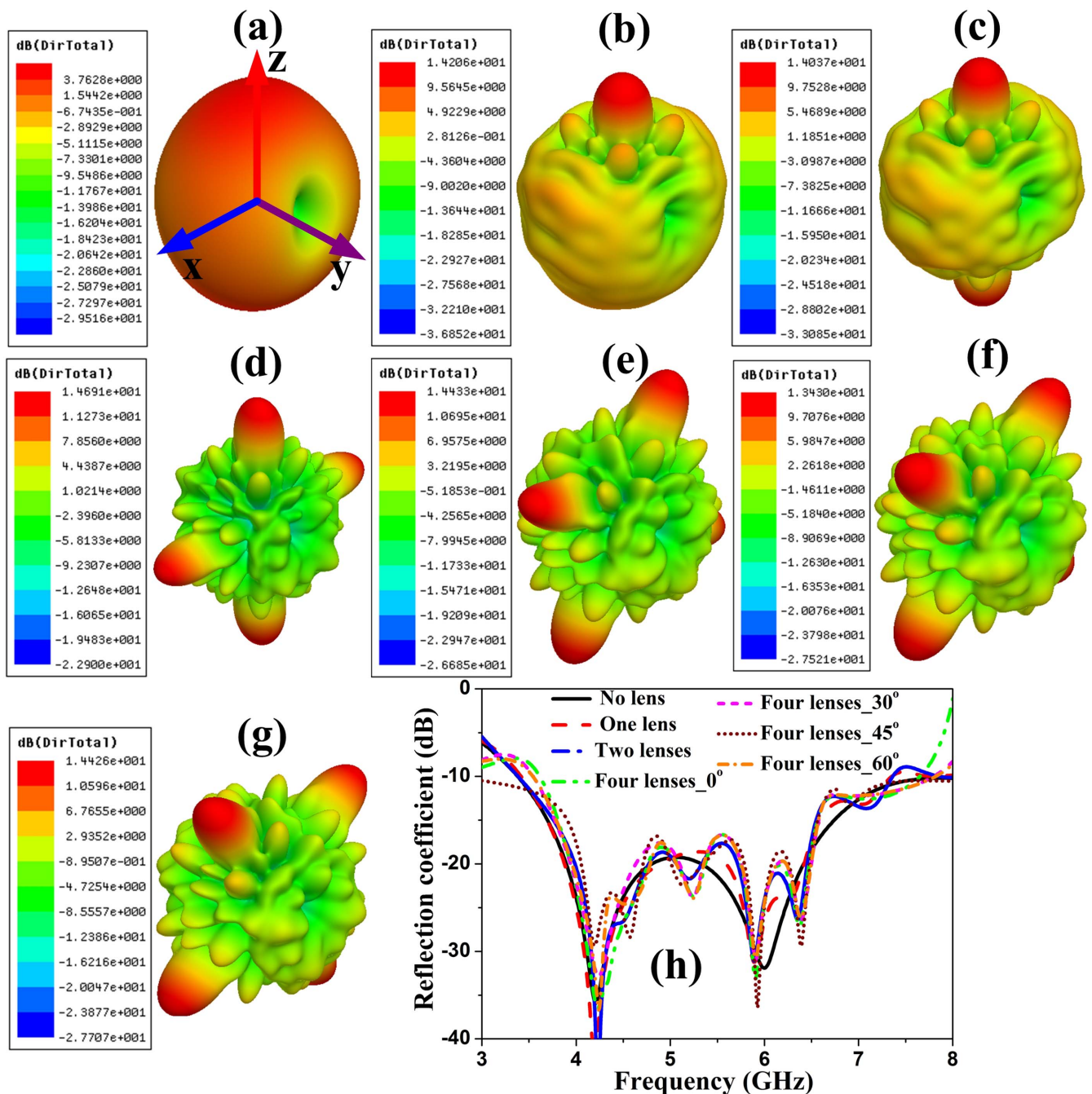


**Figure 5** | Simulated 3D far-field radiation patterns at 5.5 GHz for (a) conventional monopole, (b) single-beam, (c) two-beam, and (d–g) four-beam lens antennas with  $\theta = 0^\circ$  (d),  $\theta = 30^\circ$  (e),  $\theta = 45^\circ$  (f), and  $\theta = 60^\circ$  (g), respectively. (h) Reflection coefficients of these antennas.

**Numerical and experimental results.** To validate the design method for the lens antenna, the gain is plotted as a function of  $D$ , see Fig. S4. The maximum gain of 14 dB occurs around  $D = 90$  mm which is used to design the index gradient. Consequently, the rationality of approximating the monopole as a point source and effective design of the lens are confirmed. Higher gain of more than 19.3 dB and larger aperture efficiency are achieved at 5 GHz when a horn antenna with length of  $D = 90$  mm and aperture of the lens is employed as the source at the cost of multiple beams. This level of gain approximates to the maximum gain of 20 dB according to  $G_{\max} = 4\pi L_{\text{lens}}^2 / \lambda_0^2$  for which  $D$  should be sufficiently long. Therefore, the relative low gain of the lens antenna is attributable to the utilized omnidirectional monopole. In comparison with multi-beam emission system using several aperture antennas or arrays, our approach features moderate

antenna gain, low loss, broad band, and requires only a single feed without using complicated feeding networks such as power dividers. Moreover, the distance  $D$  in our scheme can be significantly reduced relative to the bare horn for the same level of uniform phase distribution, enabling a compact multi-beam antenna.

To demonstrate the phase-collimating capability of the GRIN lens, the aperture fields in xoy plane for antennas with and without the GRIN lens are calculated and the electric field  $E_y$  component is plotted, see Fig. S5. Clearly, desirable phase-correction functionality can be identified from the uniform phase fronts across the entire aperture except for the edge of the lens. On the contrary, the phase front suffers significant fluctuations in the bare monopole case. Notice that the variation of phase front on the lens edge poses little influence on the radiation performances since most energy radiates through the central part.

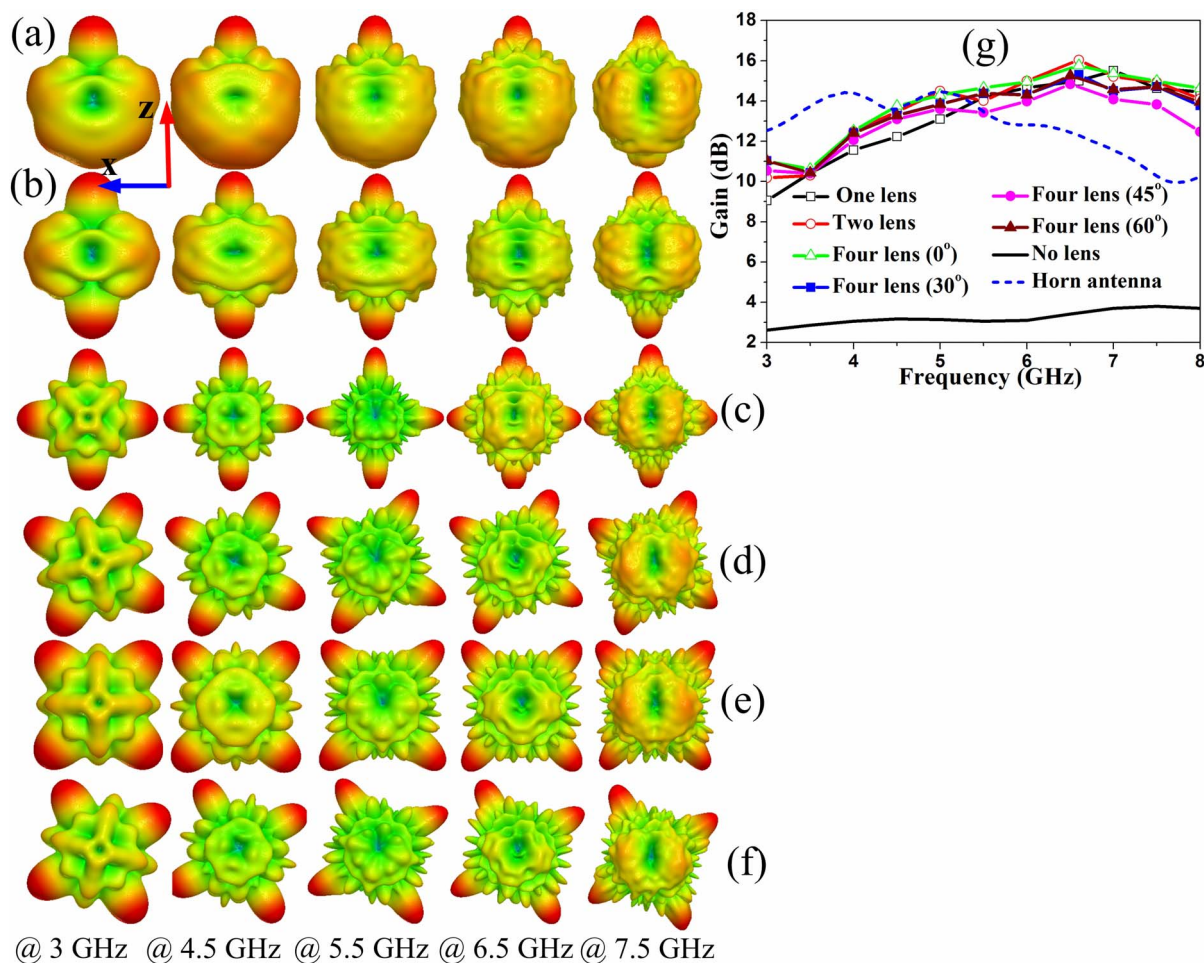


**Figure 6 | Simulated far-field radiation patterns and gain of the proposed highly-directive emission system under different scenarios.** The snapshots are plotted at different frequencies. (a) Single beam. (b) Two beams. Four beams with (c)  $\theta = 0^\circ$ , (d)  $\theta = 30^\circ$ , (e)  $\theta = 45^\circ$  and (f)  $\theta = 60^\circ$ . (g) The frequency-dependent gain of these antennas.

Fig. 5 illustrates the simulated 3D far-field radiation patterns and reflection coefficients  $S_{11}$  of the monopole with and without GRIN lenses, aiming to provide an intuitive view on the controllable highly-directive emissions. Different scenarios of single beam, two beams, and four beams are extensively examined with different directions at 5.5 GHz. As is expected from Figs. 5(a)–(g), the omnidirectional patterns of the monopole in  $xoz$  plane (H plane) are transformed to several narrow-beam patterns with high directivity. With respect to the bare printed monopole, an average of 10 dB directivity enhancement is achieved along lens directions in all cases, which is a very attractive and challenging feature. Moreover, the monopolar pattern with null radiation at broadside still holds, indicating that these lenses only rearrange the energy distribution in H plane. Most importantly, it is demonstrated for the first time that the number of beams in free space can be tailored at will and the beams can be arbitrarily directed by simply steering the orientations of the lenses from an embedded actual printed monopole. The multi-beam directive emissions deviate from the multi-beam generation in<sup>21,42,43</sup> which are still constrained to surround a ideal probe with zero-refractive-index or GRIN metamaterials in a 2D waveguide. Our multi-beam control scheme provides more versatility, flexibility and stronger signal intensity, while also maintains easy implementation in practice. From Fig. 5(h), it is learned that the lenses introduced in all cases do not deteriorate the broadband impedance-matching performance of the printed monopole, for which the  $S_{11}$  is better than  $-10$  dB from 3.5 to 7.5 GHz.

Fig. 6 gives the simulated far-field patterns in H plane and the realized gain at a number of frequencies from 3 to 8 GHz. Here, the antenna gain in all cases is calculated by taking losses into account. From Figs. 6(a)–(f), we learn that the sidelobes increase appreciably at the lower and upper edges of the passband, which is attributable to the dispersive GRIN material parameters. In this scenario, the constitutive parameters of the lens deviate slightly from the theoretically calculated ones when the frequencies deviate from the centre frequency 5.5 GHz at which the lens is exactly designed. Nevertheless, the slightly deteriorative sidelobe in the off-center band does not preclude the system from real-world applications since the directivity of main beams does not decay until 6.5 GHz. From Fig. 6 (g), an obvious gain enhancement is observed across the whole band in all cases and the minimum value is found to be 6.5 dB at 3 GHz. The gain decay at the lower frequency end is due to the size of the aperture in terms of the wavelength decreases significantly at that end, whereas the dispersive GRIN material parameters account for the raised return loss and material losses and thus give rise to the gain decay at the upper frequency end. Despite this, the radiation efficiency of the lens antenna  $\eta$  calculated as the proportion of the gain and directivity is larger than 90%, further demonstrating that the losses induced by the lens are extremely small. Moreover, the gain is very appealing and comparable with respect to aforementioned bare horn antenna, see the dashed blue curve. This is especially true for the gain at high frequencies.

To provide physical insight regarding the highly-directive emissions, the near-field mapping is performed in 3D free-space mea-

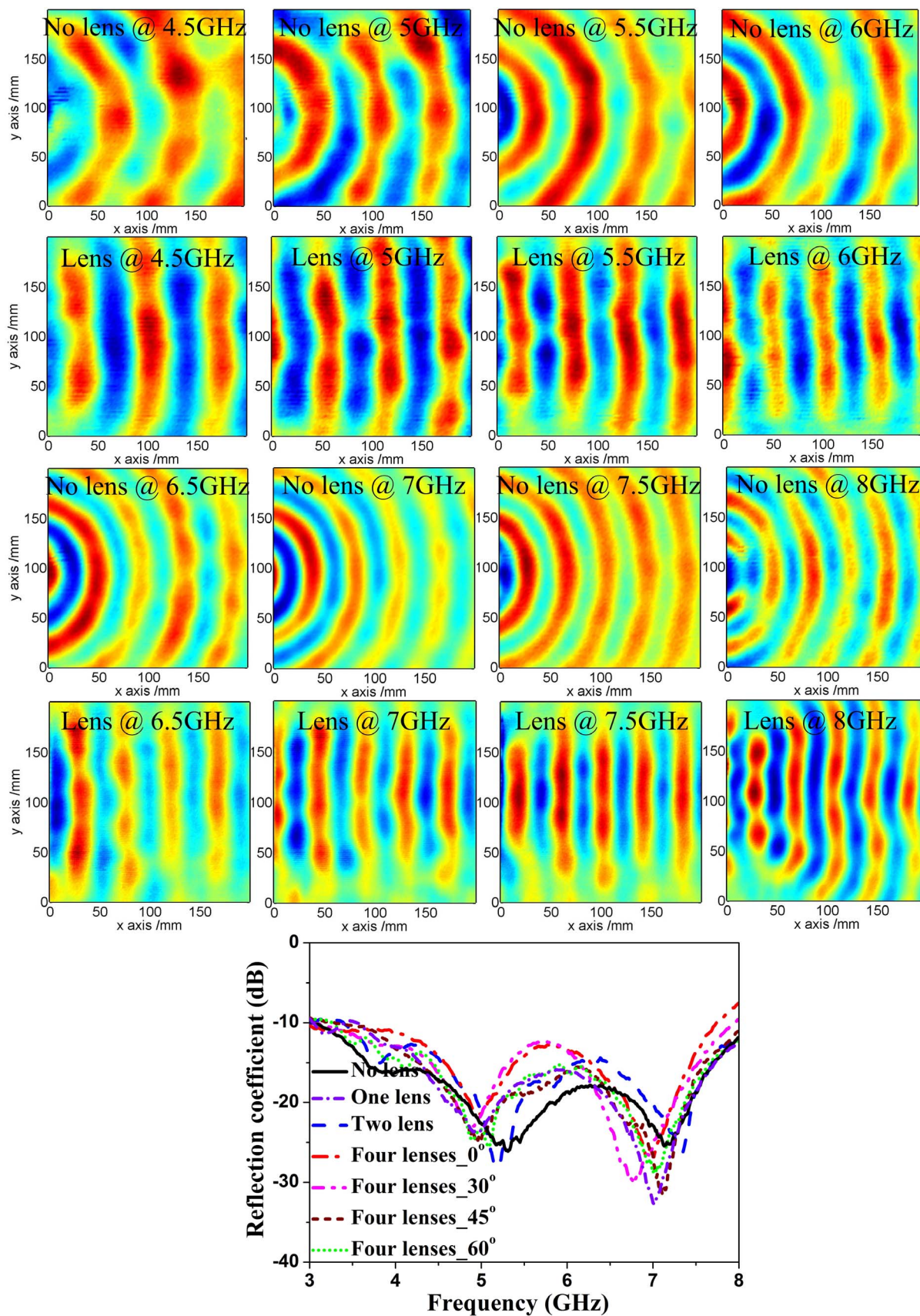
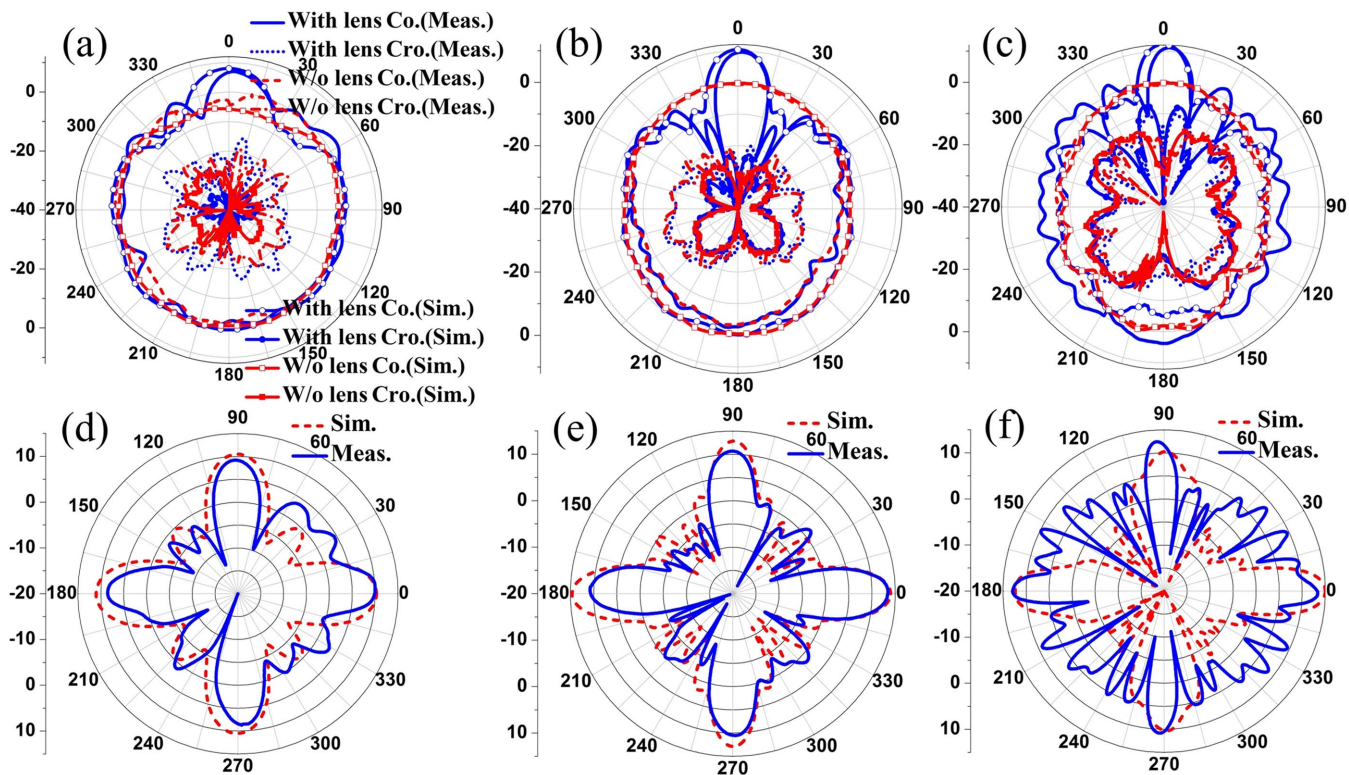


Figure 7 | Measured electric-field distributions and reflection coefficients. The snapshots are plotted in free space behind the bare monopole and lens in steps of 2 mm at several selected frequencies.



**Figure 8** | Simulated and measured radiation patterns for the (a)–(c) single-beam and (d)–(f) four-beam antenna at 3.5 GHz (the left column), 5.5 GHz (the middle column), and 7.5 GHz (the right column). Note that the results of the bare monopole (without the lens) are given for comparisons.

surement apparatus. In the experimental setup, see Fig. S6, the broadband monopole placed on an aluminum plate is 90 mm away from the GRIN lens and is embedded in foam to provide mechanical support. It functions as a transmitter and moves together with an electronic step motor automatically along two dimensions by scanning an area of  $200 \times 200 \text{ mm}^2$ . At the front side of the lens, a 1.19 mm-diameter semi-rigid coaxial probe is fixed stationary to a ferric bracket to detect the electric fields. Both transmitting and receiving antennas are connected to the two ports of a phase-sensitive network analyzer (Agilent PNA-LN5230C) via two coaxial cables and are placed at the waist of the GRIN lens to avoid truncation effects of finite lens dimension.

Fig. 7 plots the reflection coefficients and measured free-space electric-field distributions. The successful conversion of quasi-spherical waves to plane waves is clearly observed from 4.5 to 8 GHz in steps of 0.5 GHz by comparing the wavefronts outgoing from the lens antenna and bare monopole, respectively. Here, the results at the lower edge of passband are not given due to the large wavelength at these frequencies. In this regard, the long wavefront exceeds the scanning capability of available near-field measurement apparatus, making it impossible to clearly identify a complete wavefront. Nevertheless, the highly-directive emissions at these frequencies can be evidenced from the measured far-field patterns. Since the GRIN elements operate far from their resonant frequencies, the loss induced by the sample is extremely low and is hardly indicated from the measurements. Therefore, almost identical intensity can be inspected from the color maps of outgoing waves in all cases. The nonideal monopole with finite ground dimensions gives rise to the uneven and unsmooth wavefronts. Moreover, the measured reflection coefficients are in reasonable agreement with simulations, revealing that the return loss of the bare monopole and integrated lens antennas under different scenarios is better than  $-10 \text{ dB}$  from 3.2 to 7.75 GHz, which is more than an octave. Therefore, the accuracy of employing GRIN fractal elements in constructing bulk GRIN lenses is verified.

To experimentally validate the appealing far-field characteristics of the 3D antenna system, Fig. 8 compares the simulated and measured H-plane radiation patterns of both single-beam and four-beam antennas from 3.5 to 7.5 GHz in steps of 2 GHz. The radiation patterns in other frequencies can be observed from Fig. S7. All patterns are normalized to the co-polarization of the designed monopole. As is inspected, the results between simulations and measurements are in reasonable consistency. In both single-beam and four-beam cases, the gain enhancement is observed more than 10 dB along certain orientations. The measured cross-polarization radiations are at least 15 dB lower than the co-polarization ones at most frequencies and become worse at both edges of the passband. The nonuniform intensity (amplitude fluctuations) of the four main beams is attributed to the slightly broken uniformity of the monopole pattern which is induced by the insufficiently large ground plane. The appreciably higher cross-polarization radiations in experiments, and slight discrepancies of co-polarization patterns reflection coefficients (especially the shift of reflection zeros) between simulations and measurements are partially attributable to the tolerances that are inherent in fabrications, and partially to effects of supporting foam and adhesives that are not considered in simulations. Moreover, the misalignment of transmitting and receiving antennas and the nonideal background environment also account for the observed deviations. Nevertheless, these tolerances pose little influence on lens function.

## Discussion

To conclude, we have succeeded in demonstrating a highly-directive emission system which possesses the merits of broad band, low loss, high gain, and flexible beam numbers and beam directions. Numerical and experimental results are in good consistency, showing that the emission system exhibits a near 10 dB gain enhancement, and moderate cross-polarized radiations which are 15 dB lower than the co-polarized radiations over an octave in super-





extended C band. Therefore, the effective design for a broadband 3D slab lenses under the free-space excitation of a planar printed monopole and the advantages of using fractal strategy in 3D GRIN lens design without increasing the manufacturing complexity have been confirmed. The proposed scheme introduces an alternative avenue to improve the gain of microstrip antennas from a material perspective. Other omnidirectional source with uniform patterns can be employed for further improvements.

## Methods

Suppose that the aperture of the monopole is negligible with respect to that of the 3D lens, the monopole can be approximated as a point source in design and the diffraction in terms of truncation effects can be eliminated. Despite this, the design process is more complicated than 2D design by using ideal point source, which will be discussed later. Denote the thickness and side length of the lens as  $t = t_{\text{core}} + 2t_{\text{coat}}$  and  $L_{\text{lens}}$ , respectively and assume that the wave inside the lens travels parallel to the optical axis without a lean. Here,  $t_{\text{core}}$  and  $t_{\text{coat}}$  are thicknesses of the core and coat lens, respectively. To guarantee the phase-collimating performance of the lens, the optical path from the source to any point in the upper surface of the GRIN lens should be the same, yielding the same phase delay.

$$\frac{D}{\lambda_0} + \frac{n_0 t}{\lambda_0} = \frac{\sqrt{r^2 + S^2}}{\lambda_0} + \frac{n_r t}{\lambda_0} \quad (1)$$

where  $n_0$  is the refractive index at the center of the lens, and  $n_r$  is the radially distributed index as a function of radius  $r$ . Then,  $n_r$  can be immediately obtained from Eq. (1).

$$n_r = n_0 + (D - \sqrt{r^2 + D^2})/t \quad (2)$$

Although the required index of the lens is obtained, it is impossible to achieve the rigorous criterion  $\epsilon_r = \mu_r = n_r$  in broadband and there is a large index fluctuation at the interface of lens and air, resulting in a severe impedance mismatch. To relax the fluctuation and thus enable a smooth transition of index and desirable impedance matching, the aforementioned one-layer lens is substituted by a core lens sandwiched by two identical coat lenses<sup>37</sup> each functioning as a one-stage  $\lambda/4$  impedance transformer, see Fig. 2(c). To guarantee simultaneously the beam-collimating function, the optical path for the three-layer lens should meet the following criterion.

$$n_{\text{core}} t_{\text{core}} + 2n_{\text{coat}} t_{\text{coat}} = n_r t \quad (3)$$

Since the effective permeability in this particular design maintains as unity across the entire band, we have  $n_{\text{core}} = \sqrt{\epsilon_{\text{core}}}$  and  $n_{\text{coat}} = \sqrt{\epsilon_{\text{coat}}}$ . Then  $\epsilon_{\text{coat}} = \sqrt{\epsilon_{\text{core}} \epsilon_0}$  and  $n_{\text{coat}} = \sqrt{n_{\text{core}} n_0}$  can be immediately obtained by taking the one-stage  $\lambda/4$  transformer condition  $Z_{\text{coat}} = \sqrt{Z_{\text{core}} Z_0}$ . By inserting these equations into Eq. (3), the radially distributed index of the coat and core lens can be achieved after some simplifications.

$$n_{\text{coat}} = \frac{-2t_{\text{coat}} + \sqrt{4t_{\text{coat}}^2 + 4n_r t_{\text{core}} t}}{2t_{\text{core}}} \quad (4)$$

$$n_{\text{core}} = \epsilon_{\text{coat}} = n_{\text{coat}}^2$$

Here, the thickness of the coat lens can be roughly determined corresponding to  $\lambda_0/4$ , whereas that of the core lens should be designed as  $\lambda_0/2$  to guarantee desirable phase-collimating performances. In actual realizations, the 3D collimating lens is discretized into eight concentric circular regions each having a specific refractive index.  $n_0$  is cautiously chosen as  $n_0 = 1.8$  to ease the fabrications in achieving large index gradients. Since the monopole is not an ideal point source, it is hard to strictly align the radiation center of the monopole with that of the lens, making the simple ray tracing do not always hold. To make the approximation more accurately, the aperture of the lens and  $D$  should be sufficiently large and should fulfill the condition

$\sqrt{D^2 + L_{\text{lens}}^2}/4 - \sqrt{D^2 + (L_{\text{lens}} - L)^2}/4 < \sigma$  and  $\sqrt{D^2 + L^2}/4 - D < \sigma$ . The parameter  $\sigma$  defines the accuracy criterion and is chosen as  $\sigma = \lambda_0/6$  in this particular design. Moreover, the relative position (xoy plane) of the monopole relative to the lens is optimized to have a maximum peak gain for a given  $D$ . Here,  $D$  plays a crucial role in determining the antenna performances such as gain when the position of the monopole is determined. To afford efficient excitation and maximum aperture efficiency, it is designed and optimized as  $D = 90$  mm by comparing the performances of antennas with different  $D$  and index gradients. In this connection, the radiation center of the outgoing wave can be tailored at the geometrical center of the lens, which guarantees a desirable gain and directivity.

- Shelby, R. A., Smith, D. R. & Schultz, S. Experimental verification of a negative index of refraction. *Science* **292**, 77 (2001).
- Enoch, S., Tayeb, G., Sabouroux, P., Guerin, N. & Vincent, P. A metamaterial for directive emission. *Phys. Rev. Lett.* **89**, 213902 (2002).
- Song, K., Lee, S.-H., Kim, K., Hur, S. & Kim, J. Emission enhancement of sound emitters using an acoustic metamaterial cavity. *Sci. Rep.* **4**, 4165; DOI: 10.1038/srep04165 (2014).

- Pendry, J. B. Negative refraction makes a perfect lens. *Phys. Rev. Lett.* **85**, 3966 (2000).
- Xu, H.-X., Wang, G.-M., Qi, M. Q., Li, L. & Cui, T. J. Three-dimensional super lens composed of fractal left-handed materials. *Adv. Opt. Mater.* **1**, 495 (2013).
- Jiang, W. X. *et al.* Broadband all-dielectric magnifying lens for far-field high-resolution imaging. *Adv. Mater.* **25**, 6963 (2013).
- Schurig, D. *et al.* Metamaterial electromagnetic cloak at microwave frequencies. *Science* **314**, 977 (2006).
- Liu, R. *et al.* Broadband ground-plane cloak. *Science* **323**, 366 (2009).
- Landy, N. & Smith, D. R. A full-parameter unidirectional metamaterial cloak for microwaves. *Nature Mater.* **12**, 25 (2013).
- Liu, R. *et al.* Experimental demonstration of electromagnetic tunneling through an epsilon-near-zero metamaterial at microwave frequencies. *Phys. Rev. Lett.*, **100**, 023903 (2008).
- Landy, N. *et al.* Perfect metamaterial absorber. *Phys. Rev. Lett.* **100**, 207402 (2008).
- Xu, H.-X. *et al.* Triple-band polarization-insensitive wide-angle ultra-miniature metamaterial transmission line absorber. *Phys. Rev. B* **86**, 205104 (2012).
- Cao, T., Wei, C.-W., Simpson, R. E., Zhang, L. & Cryan, M. J. Broadband polarization-independent perfect absorber using a phase-change metamaterial at visible frequencies. *Sci. Rep.* **4**, 3955; DOI: 10.1038/srep03955 (2014).
- Watts, C. M., Liu, X. & Padilla, W. J. Metamaterial electromagnetic wave absorbers. *Adv. Mater.* **24**, OP98–OP120 (2012).
- Feng, S. M. Loss-induced omnidirectional bending to the normal in epsilon-near-zero metamaterials. *Phys. Rev. Lett.* **108**, 193904 (2012).
- Smith, D. R., Mock, J. J., Starr, A. F. & Schurig, D. Gradient index metamaterials. *Phys. Rev. E* **71**, 036609 (2005).
- Sun, S. L. *et al.* Gradient-index meta-surfaces as a bridge linking propagating waves and surface waves. *Nature Mater.* **11**, 426 (2012).
- Pfeiffer, C. & Grbic, A. Metamaterial Huygens' surfaces: tailoring wave fronts with reflectionless sheets. *Phys. Rev. Lett.* **110**, 197401 (2013).
- Driscoll, T. *et al.* Free-space microwave focusing by a negative-index gradient lens. *Appl. Phys. Lett.* **88**, 081101 (2006).
- Lin, X. Q. *et al.* Controlling electromagnetic waves using tunable gradient dielectric metamaterial lens. *Appl. Phys. Lett.* **92**, 131904 (2008).
- Ma, H. F., Chen, X., Yang, X. M., Jiang, W. X. & Cui, T. J. Design of multibeam scanning antennas with high gains and low sidelobes using gradient-index metamaterials. *J. Appl. Phys.* **107**, 044904 (2010).
- Cheng, Q., Ma, H. F. & Cui, T. J. Broadband planar Luneburg lens based on complementary metamaterials. *Appl. Phys. Lett.* **95**, 181901 (2009).
- Liu, R. P. *et al.* Gradient index circuit by waveguided metamaterials. *Appl. Phys. Lett.* **94**, 073506 (2009).
- Paul, O., Reinhard, B., Krolla, B., Beigang, R. & Rahm, M. Gradient index metamaterial based on slot elements. *Appl. Phys. Lett.* **96**, 241110 (2010).
- Neu, J. *et al.* Metamaterial-based gradient index lens with strong focusing in the THz frequency range. *Opt. Express* **18**, 27748 (2010).
- Kundtz, N. & Smith, D. R. Extreme-angle broadband metamaterial lens. *Nature Materials* **9**, 129 (2010).
- Zhang, Y., Mittra, R. & Hong, W. On the synthesis of a flat lens using a wideband low-reflection gradient-index metamaterial. *J. Electromagn. Waves Appl.* **25**, 2178 (2011).
- Mei, Z. L., Bai, J., Niu, T. M. & Cui, T. J. A half maxwell fish-eye lens antenna based on gradient-index metamaterials. *IEEE Trans. Antennas Propag.* **60**, 401 (2012).
- Mei, Z. L., Bai, J. & Cui, T. J. Experimental verification of a broadband planar focusing antenna based on transformation optics. *New J. Phys.* **13**, 063028 (2011).
- Dhouibi, A., Burokur, S. N., Lustrac, A. de. & Priou, A. Metamaterial-based half Maxwell fish-eye lens for broadband directive emissions. *Appl. Phys. Lett.* **102**, 024102 (2013).
- Dockrey, J. A. *et al.* Thin metamaterial Luneburg lens for surface waves. *Phys. Rev. B* **87**, 125137 (2013).
- Jiang, W. X., Qiu, C.-W., Han, T., Zhang, S. & Cui, T. J. Creation of ghost illusions using wave dynamics in metamaterials. *Adv. Funct. Mater.* **23**, 4028 (2013).
- Xu, H.-X., Wang, G.-M., Ma, K. & Cui, T. J. Superscatterer illusions without using complementary media. *Adv. Opt. Mater.* **2**, 10.1002/adom.201400011 (2014).
- Yin, M., Tian, X. Y., Wu, L. L. & Li, D. C. A Broadband and omnidirectional electromagnetic wave concentrator with gradient woodpile structure. *Opt. Express* **21**, 19082 (2013).
- Oscar, Q.-T. *et al.* Transformation optics for antennas: why limit the bandwidth with metamaterials. *Sci. Rep.* **3**, 1903; DOI: 10.1038/srep01903 (2013).
- Ma, H. F. & Cui, T. J. Three-dimensional broadband and broad-angle transformation-optics lens. *Nat. Commun.* **1**, 124 (2010).
- Chen, X., Ma, H. F., Zou, X. Y., Jiang, W. X. & Cui, T. J. Three-dimensional broadband and high-directivity lens antenna made of metamaterials. *J. Appl. Phys.* **110**, 044904 (2011).
- Crnojevic-Bengin, V., Radonic, V. & Jokanovic, B. Complementary Split Ring Resonators Using Square Sierpinski Fractal Curves. *Proceedings of the 36th European Microwave Conference* 1333 (2006).
- Xu, H.-X., Wang, G.-M., Qi, M. Q. & Xu, Z.-M. Theoretical and experimental study of the backward-wave radiation using resonant-type metamaterial transmission lines. *J. Appl. Phys.* **112**, 065222 (2012).
- Chen, H., Ran, L., Wu, B.-I., Kong, J. A. & Grzegorzczak, T. M. Crankled S-ring resonator with small electrical size. *Progress in Electromagnetics Research* **66**, 179 (2006).



41. Chen, X., Grzegorzczak, T. M., Wu, B.-I., Pacheco, J. & Kong, J. A. Robust method to retrieve the constitutive effective parameters of metamaterials. *Phys. Rev. E* **70**, 016608 (2004).
42. Cheng, Q., Jiang, W. X. & Cui, T. J. Multi-beam generations at pre-designed directions based on anisotropic zero-index metamaterials. *Appl. Phys. Lett.* **99**, 131913 (2011).
43. Jiang, Z. H., Gregory, M. D. & Werner, D. H. Experimental demonstration of a broadband transformation optics lens for highly directive multibeam emission. *Phys. Rev. B* **84**, 165111 (2011).

## Acknowledgments

This work was supported in part by the National Natural Science Foundation of China under Grant Nos. 61372034, 60990320 and 60990324, in part by the foundation for Excellent Doctoral Dissertation of Air Force Engineering University under Grant No. KGD080913001, in part by the 111 Project under Grant No. 111-2-05, and in part by National High Tech (863) Projects under Grant Nos. 2012AA030402 and 2011AA010202.

## Author contributions

H.-X.X. carried out the numerical simulations, designed, performed and interpreted the experiments and also wrote the draft manuscript, G.-M.W. supervised the design and

experiments, Z.T. contributed to the design and experimental set-up, T.J.C. supervised and interpreted the design and experiments, and revised the manuscript.

## Additional information

**Supplementary information** accompanies this paper at <http://www.nature.com/scientificreports>

**Competing financial interests:** The authors declare no competing financial interests.

**How to cite this article:** Xu, H.-X., Wang, G.-M., Tao, Z. & Cui, T.J. High-Directivity Emissions with Flexible Beam Numbers and Beam Directions Using Gradient-Refractive-Index Fractal Metamaterial. *Sci. Rep.* **4**, 5744; DOI:10.1038/srep05744 (2014).



This work is licensed under a Creative Commons Attribution-NonCommercial-NoDerivs 4.0 International License. The images or other third party material in this article are included in the article's Creative Commons license, unless indicated otherwise in the credit line; if the material is not included under the Creative Commons license, users will need to obtain permission from the license holder in order to reproduce the material. To view a copy of this license, visit <http://creativecommons.org/licenses/by-nc-nd/4.0/>